Fracture mechanisms of an environmental barrier coating under thermomechanical loadings

Ines HAMADOUCHE [*1, 3], Thibaut ARCHER[1], Pierre BEAUCHÊNE[1], Thomas VANDELLOS[2], and François HILD[3]

[1]DMAS, ONERA, Université Paris-Saclay Châtillon, France

[2]SAFRAN Ceramics, a technology platform of Safran Tech, Le Haillan, France

[3]Université Paris-Saclay, CentraleSupélec, ENS Paris-Saclay, CNRS LMPS–Laboratoire de Mécanique Paris-Saclay, Gif-sur-Yvette, France

Abstract: The introduction of environmental barrier coating (EBC) with SiC/SiC composites in hot components airplanes engines makes it essential to master their behavior in this multiphysical environment. The aim of this paper is to investigate the fracture mechanisms of a CMC/EBC system under thermomechanical loadings, in 4-point bending under thermal gradients. The thermal and mechanical loads, along with coating thickness and cooling durations, are systematically examined to highlight their effect on crack network formation. The findings reveal that temperature gradients, mechanical loads, and cooling durations significantly affect the crack network size, shape, and depth. These results highlight the damage mechanisms and may contribute to future optimization of this type of systems.

Keywords: Environmental barrier coating (EBC), thermomechanical tests, high temperature, damage mechanisms

[*]Corresponding author: ines.hamadouche@safrangroup.com

1 Introduction

To improve the efficiency of gas turbines, one strategy is to increase engine operating temperatures. For this purpose, SiC/SiC Ceramic Matrix Composites (CMCs) [1] are promising thermostructural materials to replace nickel-based super-alloys, which have reached their intrinsic limit imposed by their melting point. CMCs offer low density and have high specific strength in addition to providing increased service temperatures [2, 3]. However, SiC-based CMCs need to be protected by an Environmental Barrier Coating (EBC) to avoid surface recession due to the formation and volatilization of $\mathrm{Si(OH)_4}$ [4] under typical service environments. The first generation of coatings based on mullite and BSAS having demonstrated its limitations in terms of lifetime [5], a new family of compositions with promising properties has been identified, classified under the name of rare earth silicates, in particular scandium (Sc), lutetium (Lu), ytterbium (Yb), yttrium (Y) and erbium (Er) [6].

Several damage mechanisms of CMC/EBC systems have been identified, namely, water vapor recession [7, 8], erosion [9], CMAS (Calcium-Magnesium Alumino-Silicate) degradation [10, 11, 12], failure induced by high velocity impacts [13], spallation due to steam oxidation [14, 15] and cracks created by thermal and thermomechanical loadings [16]. Cracking of the EBC may be related to stress relaxation by creep during the thermal cycle [17]. Norton-Bailey's law is commonly used to describe secondary creep [18, 19] and depends on the temperature, the stress and the dwell time of the load. Thus, under thermal and thermomechanical loadings, but also related to residual stresses due to the manufacturing process [20], the EBC may crack at its surface (mud cracks) and through its thickness. If crack tips reach the interface, oxidation leads to the formation of silica, which forms cracks at the interface resulting in spallation of the EBC and thus the exposure of the CMC to oxidizing environment.

The development of EBCs for high-temperature applications suggests that it is essential to identify and understand their cracking mechanisms in order to control their performance on the substrate. The cracking mechanisms of EBCs have been studied mainly under uniform temperature [20]. Under thermal gradient, for instance by high heat flux, most studies have focused on fracture mechanisms of TBCs (Thermal Barrier Coating). The first studies on this topic were performed on graded thermal barrier coatings using lower heat fluxes [21, 22]. However, few studies have focused on the impact of high heat flux heating [17, 23, 24, 25].

The aim of this paper is to investigate the failure mechanisms of EBCs under thermal gradient and mechanical loading during the application of a high heat flux cycle. In particular, the impact of test parameters such as mechanical loading level, temperature level, and EBC thickness were analyzed. In the following, a 4-point bend test under CO_2 laser heating is first introduced and the instrumentation set up to monitor and analyze cracking is described. Then, the test key parameters to investigate cracking are presented and the impact of each one on the shape, extent and depth of the network is discussed.

2 Material and methods

2.1 Tested specimen

The tested specimen considered herein is a parallelepipedic (100 mm $\times$ 10 mm $\times$ t mm with t the thickness of the specimen) multilayered system. It is composed of an yttrium disilicate ($\mathrm{Y_2Si_2O_7}$) top coat deposited by thermal spray on a ceramic matrix composite (CMC CERASEP $A600$ [26]) manufactured with Hi-Nicalon SiC fibers and SiC matrix. A thin layer of bond coat made of silicon (Si) was added to improve chemical and mechanical compatibility between the ceramic coating and the substrate. The system was then heated in a furnace to stabilize the coating. For all tests, 2.7 mm of CMC and 1 mm of EBC were used (except for studying the impact of the coating thickness).

2.2 Experimental setup and performed tests

The laser setup at ONERA [27] presented in figure 1 was used to investigate the fracture mechanisms of a CMC/EBC system under thermomechanical loadings. The mechanical loading was applied using dead loads in a 4-point bend configuration. A high power (3 kW) heat flux CO_2 laser [27] heated locally the sample on the top surface of the coating, which allowed for 3D thermal gradients (in-plane and through-thickness). A middle-wave infrared (IR) camera (FLIR X6580sc MWIR $3-5$ µm with a bandpass filter of 4 µm between $300-1500$°C) on some tests and on others a long-wave IR camera (FLIR X8581 SLS LWIR $7.5-12$ µm) were used to monitor the coating surface temperature (acquiring frames at a frequency of 1 Hz). A monochromatic pyrometer Optris CTlaser G7 (with a 8 µm wavelength and a collection area

3.4 mm in diameter) measuring the maximum temperature at the coating surface has been added to ensure the reliability of thermal measurements. An acoustic emission (AE) sensor was attached to the underside of the specimen (CMC side) to detect acoustic events indicating damage occuring in the system.

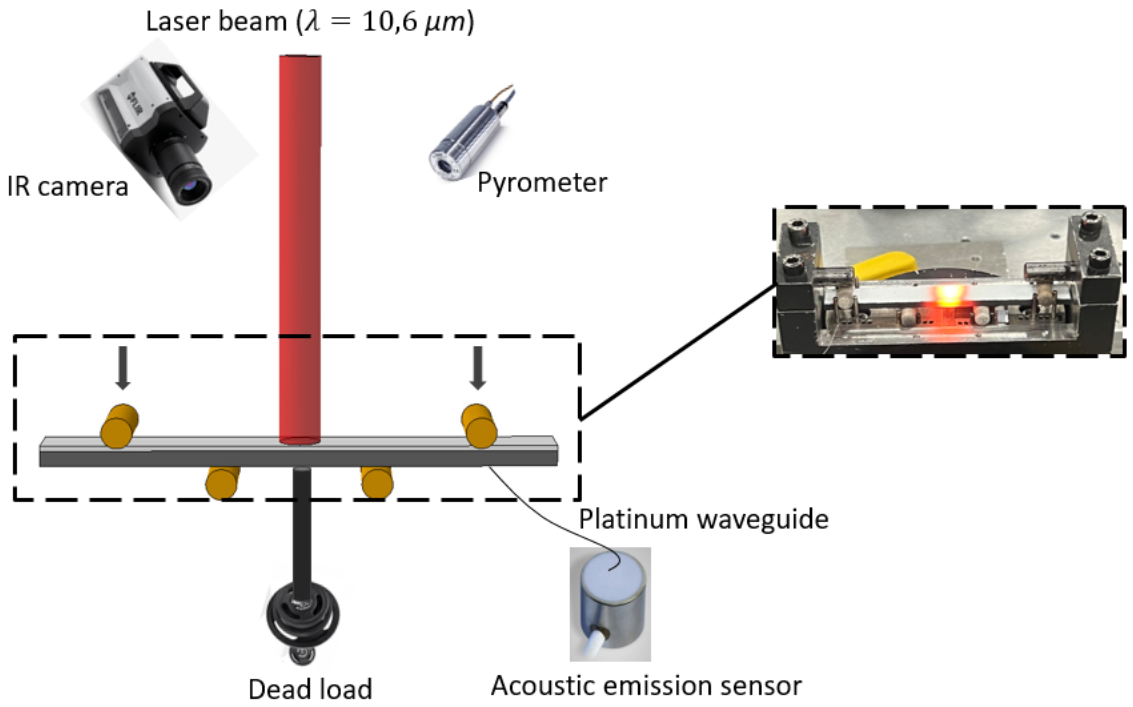

Figure 1: Experimental setup for 4-point bend test under laser loading.

The mechanical load was first applied at room temperature. Then, the thermal loading was applied at the surface center of the EBC using a ramp up to the maximum target temperature in 10 min. The laser spot size at $\frac{1}{exp^2}$ was of the order of 5 mm in diameter in the most focused case and about 8 mm in the least focused one. Then, the laser loading was maintained for 3 h to let the sample creep [27]. Last, the laser was turned off according to different cooling durations to cool down the sample.

To better understand the coating damage mechanisms, several parameters were varied to investigate the impact of each one on the formation of cracks. In this test configuration, the maximum thermal loading level, the shape of the laser spot, the mechanical loading level, the cooling duration of the laser (transition from the maximum power to 0 W) as well as the coating thickness were the parameters of interest. All tests were pre-sized to remain below the damage threshold of the system under mechanical loading alone.

2.3 Instrumentation

2.3.1 Thermal field measured by infrared camera

In order to calibrate the laser power needed to reach the desired temperature at the surface of the coating and to measure the surface temperature fields, IR measurement were performed using an MWIR (Medium wave Infrared) and an LWIR (Long wave Infrared) cameras. In order to assess true temperatures, the knowledge of the observed surface emissivity is essential. Monochromatic thermography establishes the following relationship between L_λ the spectral radiance and ε_λ the spectral emissivity

$$L_\lambda(T) = L_\lambda^0(T_R) = \varepsilon_\lambda(T) L_\lambda^0(T) \tag{1}$$

where T is the true temperature, T_R the blackbody temperature and L_λ^0 the blackbody spectral radiance. The emissivity measurements are based on characterizations at a wavelength of 4 µm and 9 µm (wavelengths of the measurements by the two IR cameras) [27]. By neglecting the flux from the environment (tests at very high temperature) and from the camera casing (thermal equilibrium of the camera since it is cooled) and by expressing the flux of the surface by Planck's law (using a monochromatic bandpass filter), it is possible to obtain the following expression

$$U = p \times \left[\frac{C_1 \lambda^{-5}}{\exp^{\frac{C_2}{\lambda T}} - 1} \right] \times IT + U_0 \tag{2}$$

where U is the measured digital level (DL), p and U_0 are constants to identify, C_1 and C_2 the parameters of Planck's equation and IT the integration time.

Last, depending on the used filter, adding the emissivity to the wavelength of the filter allows the measured level to be expressed as

$$U = p \times \left[\varepsilon(\lambda, T) \frac{C_1 \lambda^{-5}}{\exp^{\frac{C_2}{\lambda T}} - 1} \right] \times IT + U_0 \tag{3}$$

2.3.2 Acoustic emission

Since crack initiation and propagation are sources of acoustic events, this *in-situ* non-destructive testing technique [29] was used to determine the instants at which cracking occurred. The acoustic emission technique known as "discrete" has been considered in this study. A plat-

inum wire was chosen as waveguide [31]. Chemical bonding was used to couple the platinum wire to the back side (CMC) of the specimen by melting borosilicate glass above the wire in an oven. The thermal cycle was performed with a 10°C per min ramp up to 1050°C, a 3 h hold time and a 10°C per min cooling down. A Micro80 Physical Acoustics resonant sensor was chosen for its sensitivity to weak acoustic signals. Once the specimen was placed in the experimental setup, the waveguide was attached to the acoustic emission sensor with a teflon rubber band. Silicon gel [32] was added between them to ensure contact. Pencil lead breaks were performed on the coating surface (before testing) to check for the well-functioning of the method. In the present case, signals with amplitudes ranging from 55 to 80 dB were captured, enabling the method to be validated. AE monitoring was carried out in real time during the test. An energy filter (values above 10 mV.s were kept) and an amplitude filter (values above 35 dB were retained) were applied. Monitoring was continuous during the test, and a signal was emitted only when the set thresholds in energy and amplitude were exceeded. Thus, a point corresponds to a wave exceeding the set thresholds and is recorded by the transducer. The acoustic energy was normalized by the sum of the acoustic events.

In this study, AE was only used to detect damage initiation. The sensitivity of the method was too low to obtain enough signal enabling the various wave parameters to be studied.

2.3.3 Scanning electron micrographies

The samples were analyzed by SEM (MIRA3 TESCAN) in order to visualize the presence of damage recorded by acoustic emission. SEM observations were performed with the Back Scattered Electron (BSE) mode to obtain high-resolution images showing the composition of the layer. The purpose was to detect cracks in the coating, the primary beam was used with a low acceleration voltage (5 kV). First, highly resolved images (1024 px $\times$ 1024 px corresponding to a size of 781 µm $\times$ 781 µm) were acquired to make the crack path identification easier (figure 2(b)). Then, a stiching process was used to reconstruct the crack network on a larger image using these images as illustrated in figure 2(c). In addition, to help with network visualization, cracks were highlighted in black.

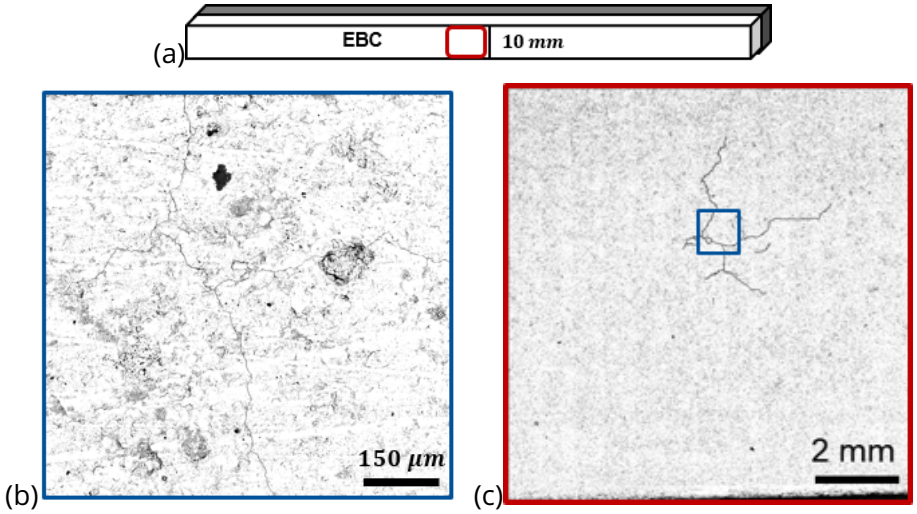

Figure 2: (a) Central area of the coating surface observed by SEM after a thermomechanical loading cycle. (b) High magnification of an image used for the cartography of cracks. (c) Cartography of hand drawn crack network in black.

2.4 Modeling

The model used was based on the geometry of the specimens. However, since the thermal loading was assumed to be centered on the EBC face, mechanical loading consisted of a 4-point bending configuration, with the CMC frame superimposed on the specimen frame, planes of symmetry along the $\underline{x}$ and $\underline{y}$ directions were defined, and only a quarter of the specimen was modeled (50 mm $\times$ 5 mm $\times$ e mm, e being the thickness of the system and dependent on the thickness of the coating) as shown in figure 3. The SiC/SiC CMC substrate was considered homogeneous with a transversely isotropic elastic behavior. The mesh was converged and based on a quadratic interpolation functions with C3D20RT-type elements, which enable deformations resulting from temperature variations to be modeled, as well as coupled thermal/mechanical analyse.

The mechanical loading was load controlled. A "reference point" was assigned to the nodes line corresponding to the upper support (the support to which the experimental mechanical loading was applied). The force was then applied at this "reference point" and evenly distributed over the entire line of nodes. At the lower support, rotation and vertical displacement were blocked to avoid rigid body motions.

The thermal loading was applied to the upper face (EBC face) using a Gaussian flux $\Phi_T(X, Y)$ dependent on position (X, Y) and expressed as

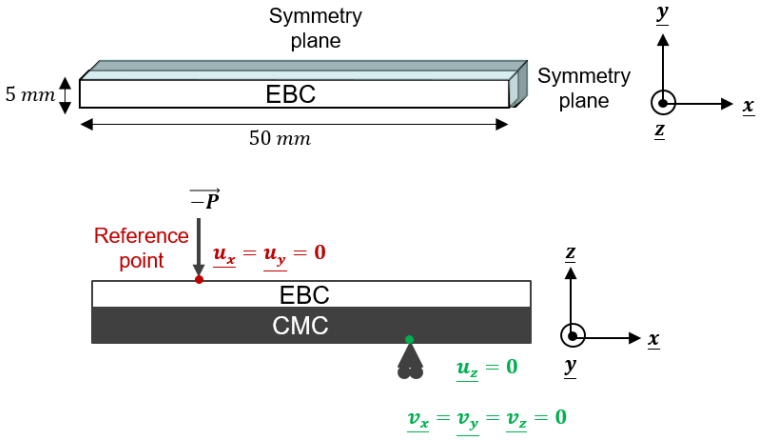

Figure 3: Geometry and boundary conditions of the thermomechanical model.

$$\Phi_T(X,Y) = A\ \exp\left[-\left(\frac{(X-X_0)^n}{B_X} + \frac{(Y-Y_0)^n}{B_Y}\right)\right] \tag{4}$$

with A the amplitude of the Gaussian flux, (X_0, Y_0) its center, B_X and B_Y the widths along the $\underline{x}$ and $\underline{y}$ directions and n the shape of the Gaussian. In ABAQUS, the heat flux was applied via a *DSFLUX subroutine.

A temperature-dependent radiation conditions r were applied to all external faces of the system. In addition, convection exchanges were modeled by a temperature-dependent convection parameter h on the front and rear faces. In the region of the alumina supports, no heat loss was considered.

The thermoelastoviscoplastic behavior of the coating and the transversely isotropic thermoelastic behavior of the CMC were taken into account. In the case of the coating, its nonlinear behavior was due to creep. A Norton-Bailey law, commonly used to describe creep of this type of coating [19, 17, 27] was used. This law relates the equivalent (Von Mises) creep strain $\bar{\varepsilon}^{cr}$ to the equivalent (Von Mises) applied stress $\bar{\sigma}$, temperature T and time t.

$$\bar{\varepsilon}^{cr} = A(T) \times \bar{\sigma}^n \times t^m \tag{5}$$

with n the stress exponent, and m the time exponent, both material dependant parameters. In this law, $A(T)$ is a velocity coefficient expressed according to Arrhenius law

$$A(T) = A_0 \times \exp(\frac{-E_a}{RT}) \tag{6}$$

with R the universal gas constant, E_a the creep activation energy and A_0 a pre-exponential factor.

For modeling purposes, a strain-hardening formulation was chosen

$$\dot{\bar{\varepsilon}}^{cr} = (A\bar{q}^n[(m+1)\bar{\varepsilon}^{cr}]^m)^{\frac{1}{m+1}} \tag{7}$$

with $\dot{\bar{\varepsilon}}^{cr}$ the equivalent creep strain rate, $\bar{q}$ the equivalent deviatoric stress and $\bar{\varepsilon}^{cr}$ the equivalent creep strain.

It is indeed creep that we wish to model, but we do so on the basis of the Strain-hardening law, as experience shows that we have better agreement with the results when the stress is not fixed during the test [28] (which is our case).

An example of a mesh, for a 1 mm thick coating, is shown in figure 4. Analyses of the various models revealed a low level of stress in mesh elements located far from the hottest point and bending supports (maximum principal stress σ_1 between 0 and 30 MPa). Thus, only the elements located in the central zone ($L < 18$ mm) were analyzed. In addition, the reference frame was defined similarly to the global frame (1 in the $\underline{x}$ direction, 2 in the $\underline{y}$ direction and 3 in the $\underline{z}$ direction).

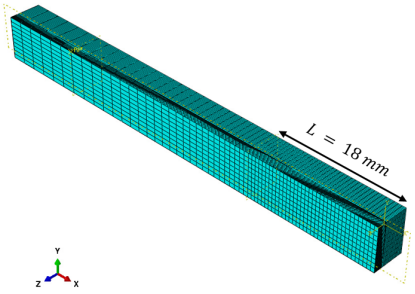

Figure 4: Mesh of a quarter CMC/EBC model with a 1 mm coating.

The coating represented the top layer of the system. In this configuration, at room temperature and under 4-point bending, the coating was in a slightly compressed state, whereas

at high temperatures, the coating was in a highly compressed state. Figure 5 shows the evolution of the maximum principal stress at the hottest point of the coating surface during a thermal cycle. The first 600 s represent the temperature rise, the following 10800 s correspond to the thermal stage, followed by cooling.

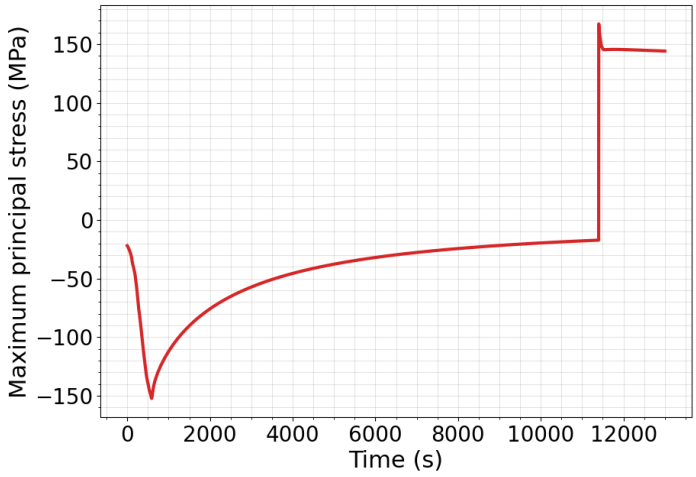

Figure 5: Change of the maximum principal stress at the hottest point of the coating surface during a thermal cycle.

The model material parameters are presented in Appendix 1.

3 Impact of experimental parameters on EBC cracking

3.1 Effect of mechanical load

One of the tested parameters that may affect coating cracking is the mechanical loading. To determine its impact, the maximum temperature level was set to 1250°C since coating creep was assumed to activate for temperatures greater than 1000°C [33]. The laser was positioned to heat the coating center surface. A first case without mechanical loading was carried out. For the following two cases, dead weights of 9 and 11 kg were selected. For the three samples, the cooling duration was quasi instantaneous. Instantaneous cooling consisted in switching from maximum laser power (the value required to achieve the target temperature at the hottest point of the coating surface) to zero power, instantaneously.

Temperature field at the coating surface

For the three cases, only one laser beam shape was used to generate the temperature field displayed in figure 6 with a low gradient along the specimen width and a large central area

exceeding a temperature level of 1200°C, thus maximizing creep.

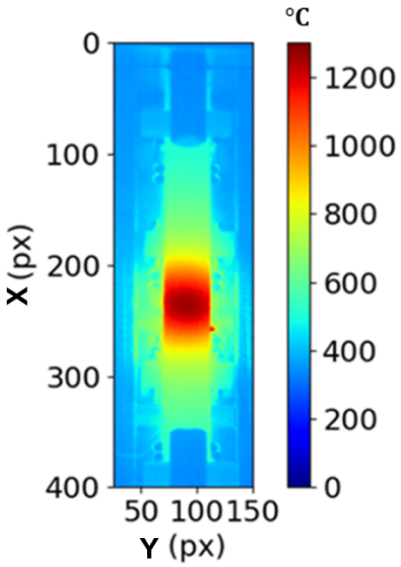

Figure 6: Temperature field at the coating surface for a maximum level of 1250°C.

Acoustic emission

Normalized cumulative energy and laser power are plotted in figure 7 for the two cases with dead weights. For the case without mechanical loading, the specimen was not equipped with acoustic emission. The two figures show that no events were detected during mechanical loading. Once the thermal loading was applied, acoustic events were observed during the cooling process in both cases.

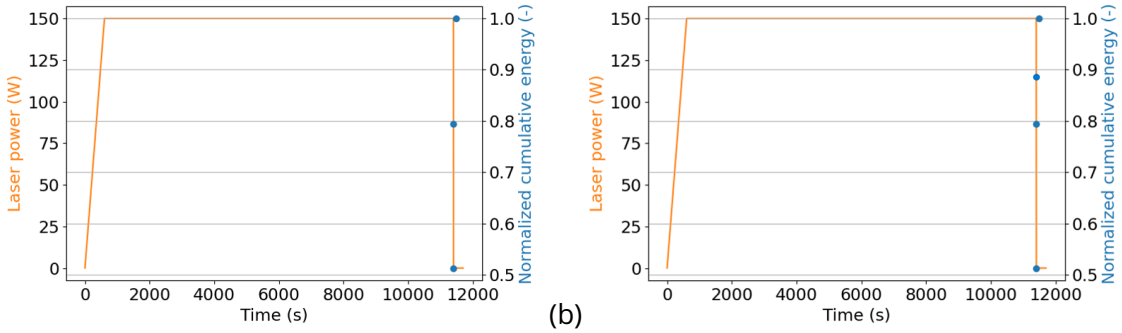

(a) (b)

Figure 7: Acoustic emission during the first thermomechanical loading cycle for the case with (a) 9 kg, (b) 11 kg.

SEM observations

SEM observations confirmed cracking within the central area of the coating surface (figure 8(a)) detected by acoustic emission during cooling. When the mechanical loading was increased, the crack network shape on the surface of the coating changed. In the reference case (figure 8(b)) when no weight was put on the assembly, the network had a circular shape, presented 9 large meshes and extended over a surface of 6.3×6.3 mm. Then, with a dead load of 9 kg (figure 8(c)), the network had a circular shape while with a dead load of 11 kg (figure 8(d)) the network had a circular part and another one with a crack that crossed the entire width of the sample to its edges. This second network was as extended as the first one along the length (8.1 mm) but larger than the first one along the width due to the crack that reached the edges. In terms of cell number, this second network had only 3 closed cells versus 13 for the first one, with a larger diameter (about 2.5 mm vs 1.5 mm). Thus, for the lowest mechanical loads (0 and 9 kg), the crack network shape was driven by thermal loading. At higher mechanical load (11 kg), the crack network shape is also driven by the 4-point bend loading.

The network generated by a mechanical load of 11 kg was more critical with respect to the lifetime of the system compared to the network generated by a mechanical load of 9 kg. The cross-sectional observation of the system (figure 9(a)) shows that the crack reaching the edges of the sample also propagated toward the interface of the system (figure 9(c)), thus creating a pathway to oxidizing species encountered in engine environment, and weakening the durability of the coating on the CMC. For lower mechanical loads, it is not the case. For 0 and 9 kg, the surface crack network was circular and not very deep (figure 9(b)).

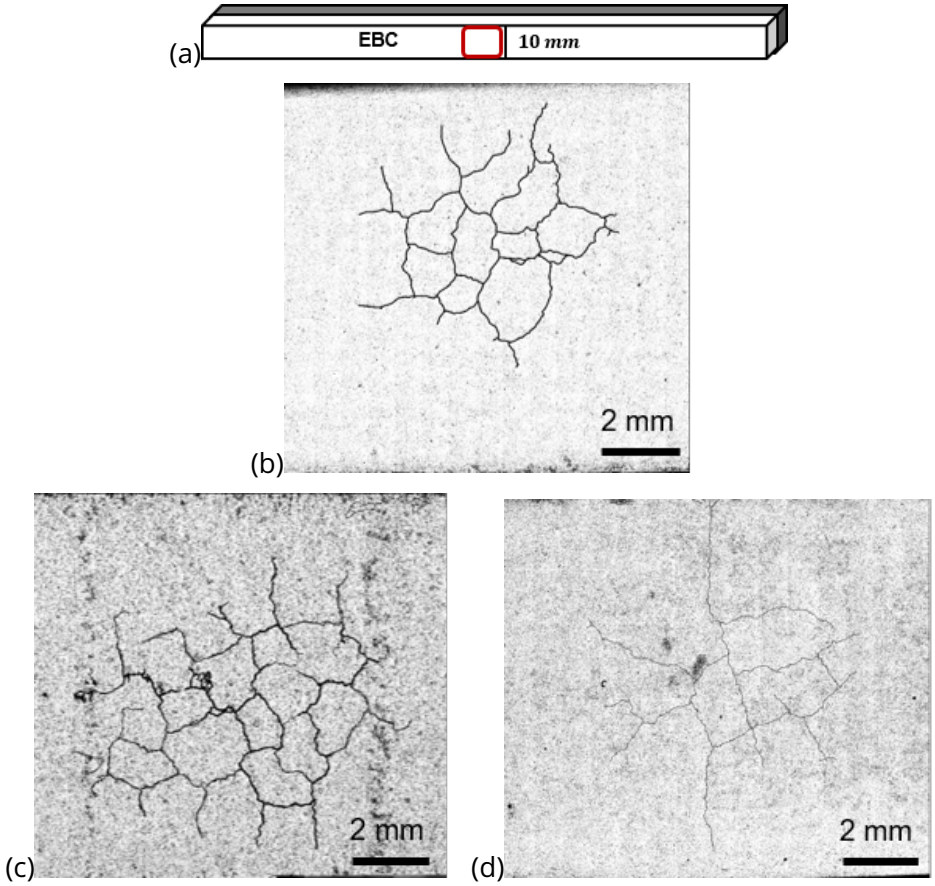

Figure 8: (a) Central area of the coating surface observed by SEM after the first thermomechanical loading cycle, (b) without load, (c) for a dead load of 9 kg and (d) 11 kg.

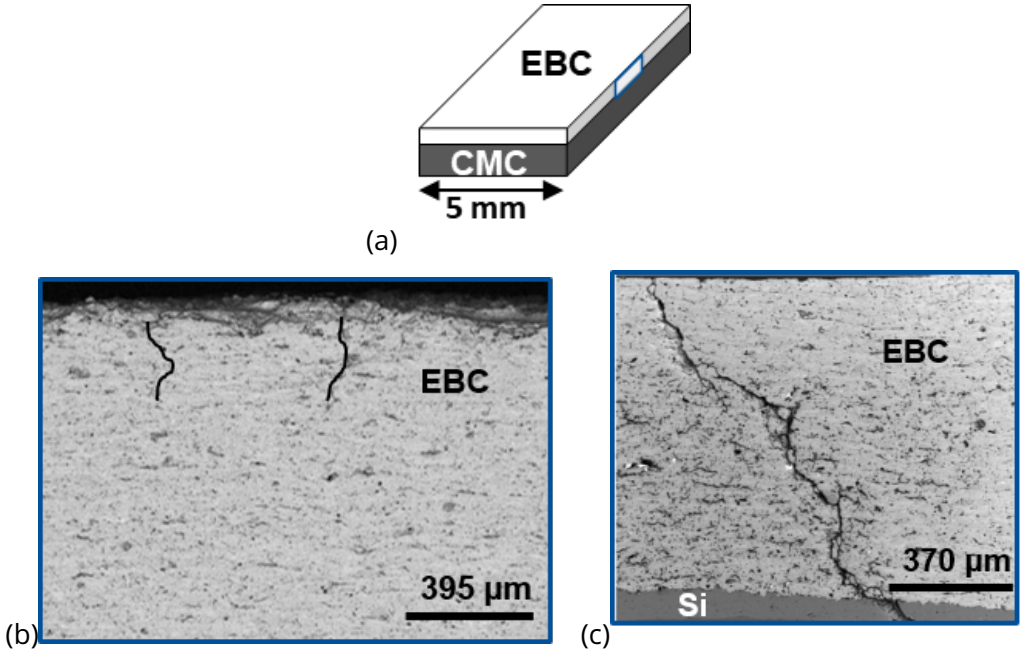

Figure 9: (a) Cross-section of the area observed by SEM after the first thermomechanical loading cycle. (b) Cross-section of the crack from a circular surface network (cases with 0 and 9 kg). (c) Through-crack (11 kg).

Thus, the study of the mechanical load impact allows its influence to be highlighted on the

shape of the network, the number and size of generated cells, and in particular, the occurrence of cracks crossing the width and propagating to the system interface, which can be a critical mechanism for the lifetime of the system.

3.2 Impact of temperature level

Two temperature levels were investigated, namely 1100°C and 1250°C with the same laser beam shape. In both cases, the mechanical load was set to 9 kg. At the end of the thermal stage, the laser beam was stopped quasi instantaneously.

Temperature field at coating surface

The temperature field, obtained at the coating surface, which was maintained for the whole thermal stage, is shown in figure 10 for both applied temperature levels. In both cases, the thermal gradient along the central zone width was very small. Furthermore, the area exceeding a temperature level of 1000°C, which is the temperature at which coating creep was assumed to activate [33], was higher in case (b) than in case (a). Thus, a larger area appears to have crept in case (b). This observation was made on the basis of the temperature level at which creep is activated. In case (b), a larger area exceeded the creep-activating temperature than in case (a). The coating creep activation and the link established between the hottest central area on the coating surface and the area that has crept were based on the work of Archer et al. [27]. The same system and heating method were used herein.

Moreover, figure 11 presents the temperature profiles along the specimen length and width. First, along the length (figure 11(a)), the area exceeding 1000°C covered approximately 32 px (about 7.6 mm) for the low temperature level and over 60 px (or 14.3 mm) for the high temperature level. This observation implies that a larger area had crept in case (b) compared to case (a). Second, it confirms that the thermal gradient along the width in both cases was small (figure 11(b)).

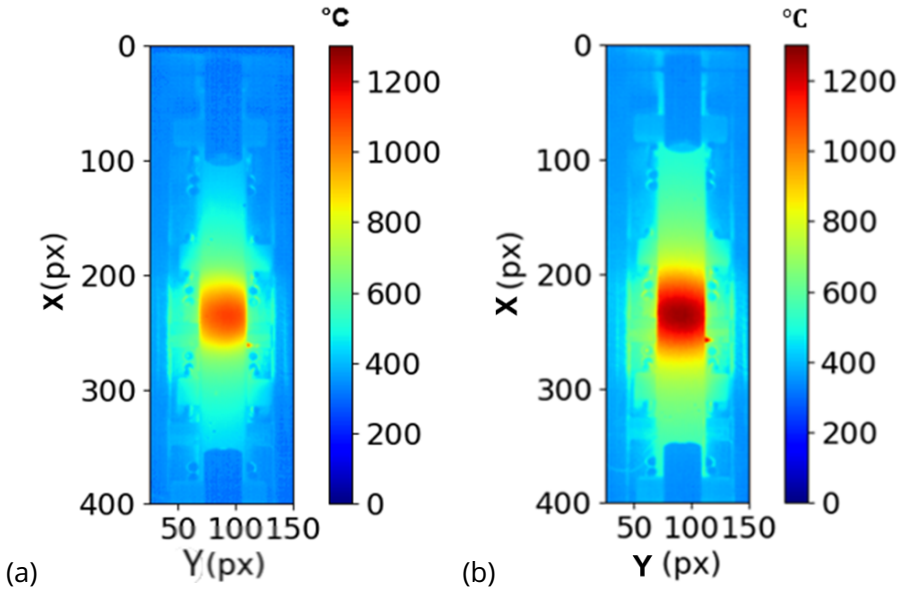

Figure 10: Temperature field at the coating surface, for a maximum temperature level of (a) 1100°C and (b) 1250°C.

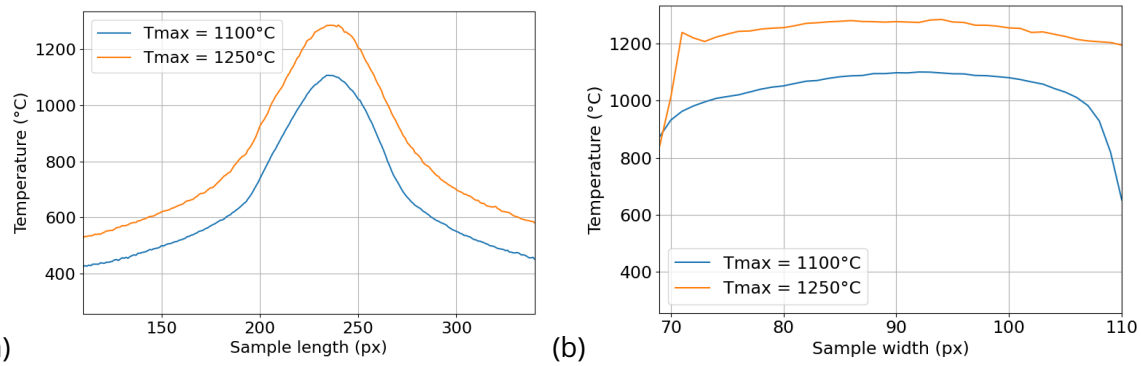

Figure 11: Temperature profiles for the 2 samples, along the (a) length, (b) width for maximum temperature levels of 1100°C and 1250°C.

Acoustic emission

The normalized cumulative energy and laser power are plotted in figure 12. For both temperature levels, no events were detected during mechanical loading. Once the thermal loading was applied, acoustic events were observed during the cooling process in the case of a maximum temperature of 1250°C. For the first case (1100°C), no events were recorded by the acoustic sensor. This result shows that the temperature level and thus the creep level had an impact on the system damage.

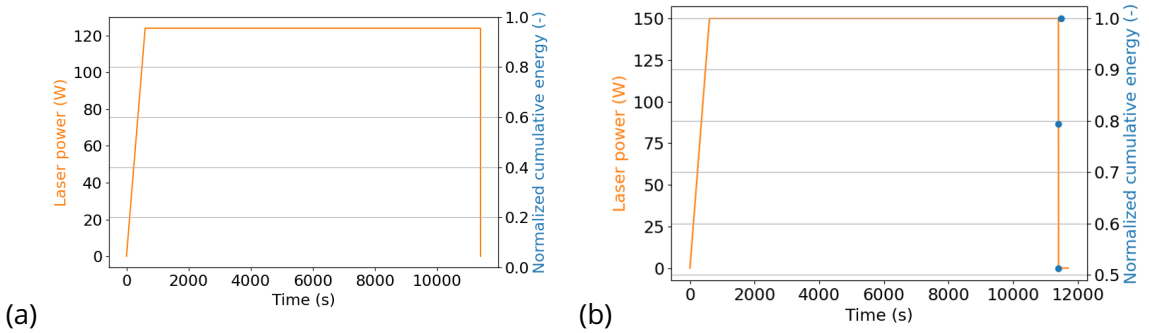

Figure 12: Acoustic emission during the first thermomechanical loading cycle for a maximum temperature of (a) 1100°C (b) 1250°C.

SEM observations

The central area of the coating surface was observed by SEM (figure 13(a)). In both cases, the SiC/SiC substrate did not exhibit damage. For the lower temperature, figure 13(b), the coating presented an incomplete crack network located at the region subjected to the laser beam, over an area of 4.2 mm $\times$ 4.2 mm. The network was slightly off-center with no specific shape. In this case, the acoustic emission did not detect any event since it was the beginning of cracking. The level of acoustic events was therefore not significant enough to be detectable. Moreover, a crack network was formed on the surface of the coating that had been loaded at 1250°C (figure 13(c)) in the area illuminated by the laser beam. The formed network was more extensive than the previous one, with a surface of 8.1 mm $\times$ 8.1 mm. Its shape was circular with 13 closed cells of an average diameter of 1.5 mm.

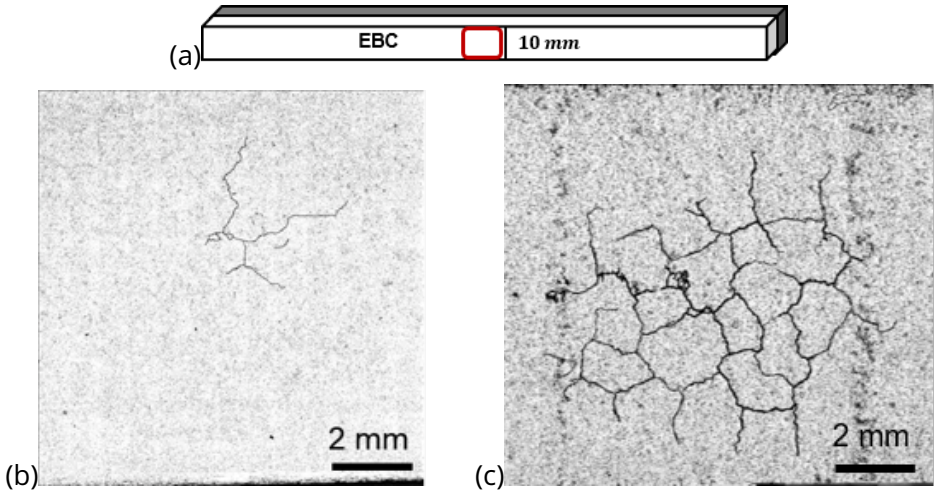

Figure 13: (a) Central area of the coating surface observed by SEM after the first thermomechanical loading cycle for a maximum temperature of (b) 1100°C and (c) 1250°C.

Through the variation of the maximum temperature level, considering the same laser beam shape, mechanical loading level and instantaneous cooling, it appears that the former pa-

rameter had a strong influence on coating damage. When the temperature of the central area ranged between 1000°C and 1100°C, cracking generated on the surface of the coating was limited and very localized. For a higher temperature level, the central zone whose temperature exceeded 1200°C (or even a more extended central zone which exceeded 1000°C), coating damage was detected during cooling and easily revealed by SEM observations since the network was richer in terms of cells and more extended.

Finite element analysis

Figure 14 shows the evolution of the creep strain during the thermomechanical cycle. The strain is plotted at the hottest element of the coating surface. The creep strain over one cycle was larger for the highest temperature.

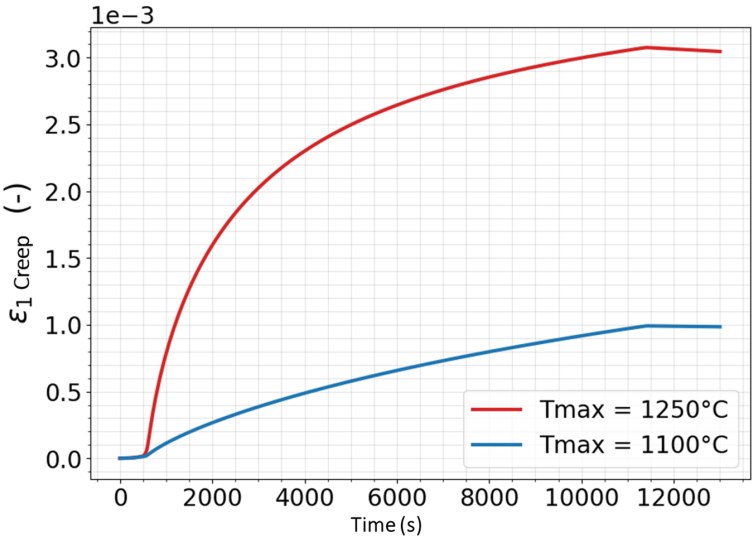

Figure 14: Evolution of maximum principal creep strain in the hottest element of the coating surface, over the thermal cycle and for the two maximum temperatures.

3.3 Impact of temperature profile

Since the thermal loading had a significant impact on coating damage, this parameter was further investigated by working on a temperature range greater than 1250°C at the hottest point (more favorable to the development of a crack network since the creep level of the system depends on the temperature level) and by varying the laser beam shape to vary the thermal gradients. The mechanical loading was kept at 9 kg and the cooling was almost instantaneous as in the previous cases.

Temperature field at the coating surface

Figure 15 displays the two temperature fields used for these cases. The two temperature fields underline the fact that the laser beam used in each case was different. The first one is the case presented above. The second one is a little more off-center than the first one. In both cases, the central area exceeding 1000°C was extended and the thermal gradient along the width was very small.

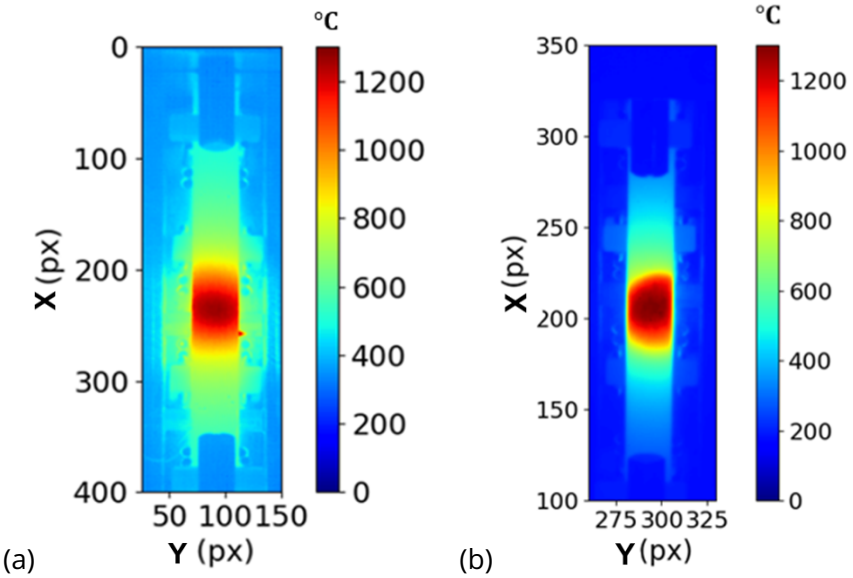

Figure 15: Temperature field at the coating surface for two laser spot shapes.

Acoustic emission

For both thermal loading shapes, acoustic events were detected upon cooling (figure 16) in accordance with those observed for several levels of thermal loading (figure 12, the two curves were exactly the same, thus a single one is shown.)

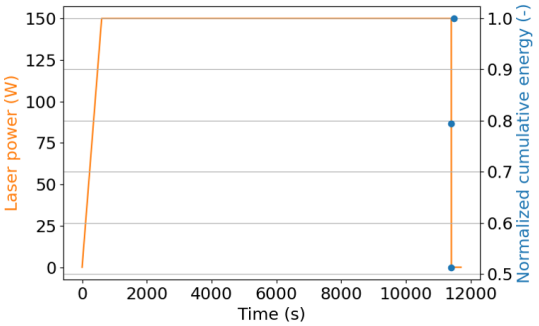

Figure 16: Acoustic emission during the first thermomechanical loading cycle for both laser beam shapes.

SEM observations

Damage detected by acoustic emission was confirmed by SEM observations on the coating surface (figure 17(a)) in both cases. The network exhibited a circular shape in both cases. However, the network was more developed in the second case (figure 17(c)). The first network (figure 17(b)) extended over an area of 8.1 mm $\times$ 8.1 mm while the second one covered an area of 10.6 mm in length and 9 mm in width. While the first network contained 13 closed cells with an average diameter of 1.5 mm, the second contained 19 with an average diameter of 2 mm.

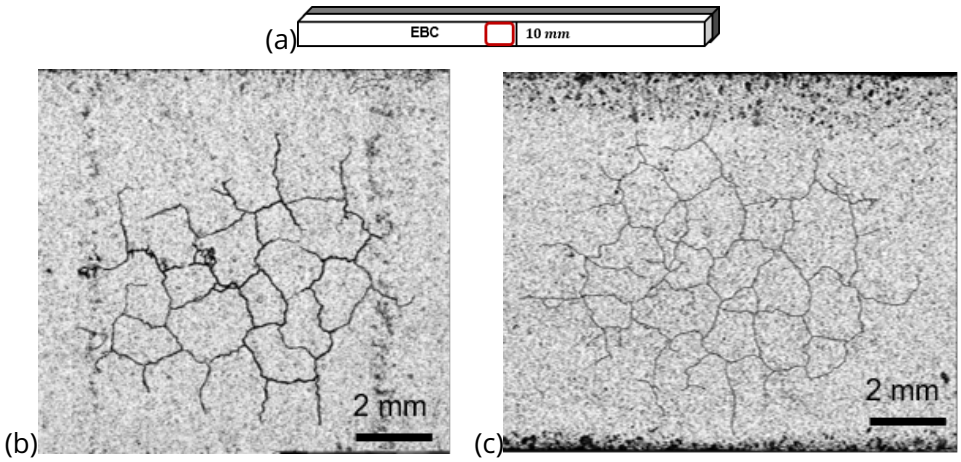

Figure 17: (a) Central area of the coating surface observed by SEM after the first thermomechanical loading cycle for (b) the first and (c) second laser beam shapes.

The results observed by varying the shape of the laser beam highlighted that this parameter had an impact on the crack network. The more the beam covered a large area, the more the cracked surface was important, and the more the number of cells was large. In the case of the second beam shape (figure 15(b)), the crack network covered almost the entire width of the sample (9 mm of cracks over 10 mm of sample width). This result is directly related to the thermal gradient across the sample width. The larger the beam and the larger the area it covered, the smaller the gradient across the width and the more extensive the crack network. This effect is linked to the size of the area in which creep activated, thereby leading to cracking.

3.4 Impact of cooling duration

The three cases studied previously all revealed, through the monitoring of the acoustic events, that coating damage occurred during the cooling stage. Thus, the effect of the cooling duration was investigated by setting the maximum temperature to 1250°C, the mechanical load

to 9 kg and by using 2 cooling durations, namely, 15 min and 2 h. The choice of different cooling ramps was guided by the creep activation time. In the instantaneous case, creep had no time to activate, while in the case of a 2 h cooling, the duration was long enough to activate creep. The 15 min duration represented an intermediate case.

Temperature field at coating surface

The temperature field measured at the surface of the coating is the same as that in figure 15(b).

Acoustic emission

Acoustic events were monitored both for the instantaneous case and for the slower coolings (figure 18). In all three situations, damage occurred during cooling. The slower the cooling ramp, the later the acoustic events.

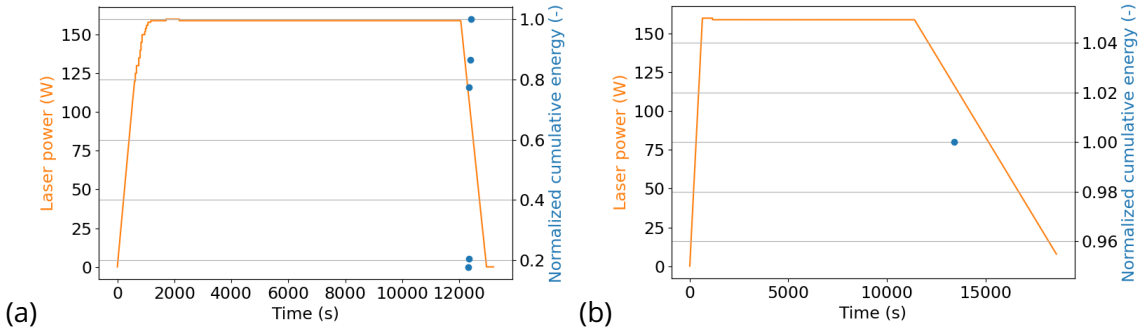

Figure 18: Acoustic emission during the first thermomechanical loading cycle, for (a) 15 min and (b) 2 h cooling.

SEM observations

In both cases, as shown in figure 19, the shape of the crack network on the top surface was the same. A circular network was close to the Gaussian shape of the laser beam used to heat the coating. The cracks all joined to form cells. There were no horizontal or vertical cracks. The overall size of the network was about 10.4 mm $\times$ 9 mm for the 15 min cooling and about 9.2 mm $\times$ 8.3 mm for the 2 h cooling. In terms of number of closed cells, the first network contained 22 and the second one 23.

Although on the surface of the coating the formed network was the same, observations of the cross-section revealed that the depth of the network was diffrent. The shorter the cool-

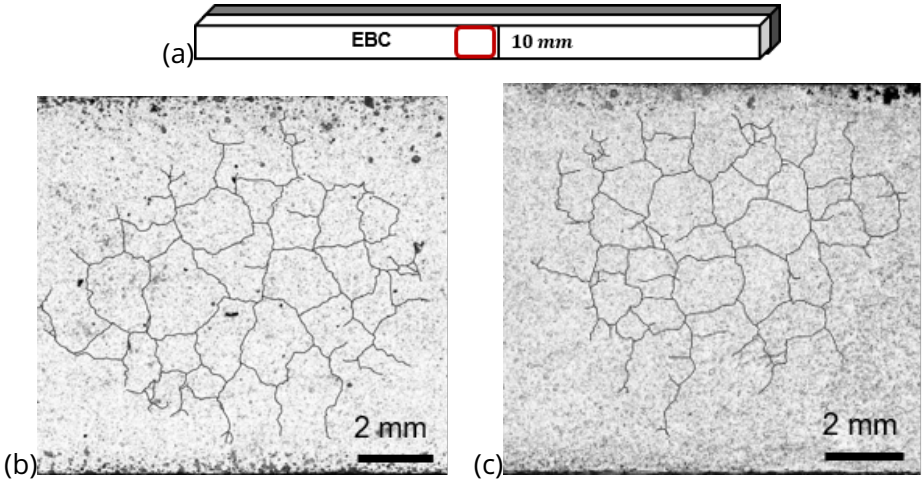

Figure 19: (a) Central area of the coating surface observed by SEM after the first thermomechanical loading cycle for (b) 15 min and (c) 2 h cooling.

ing duration, the shallower the network (figure 20). In the first case (almost instantaneous cooling), several cracks exceeded half the thickness. In the second case (15 min), some cracks propagated to almost half the thickness, while in the third case, the network barely reached a third of the thickness.

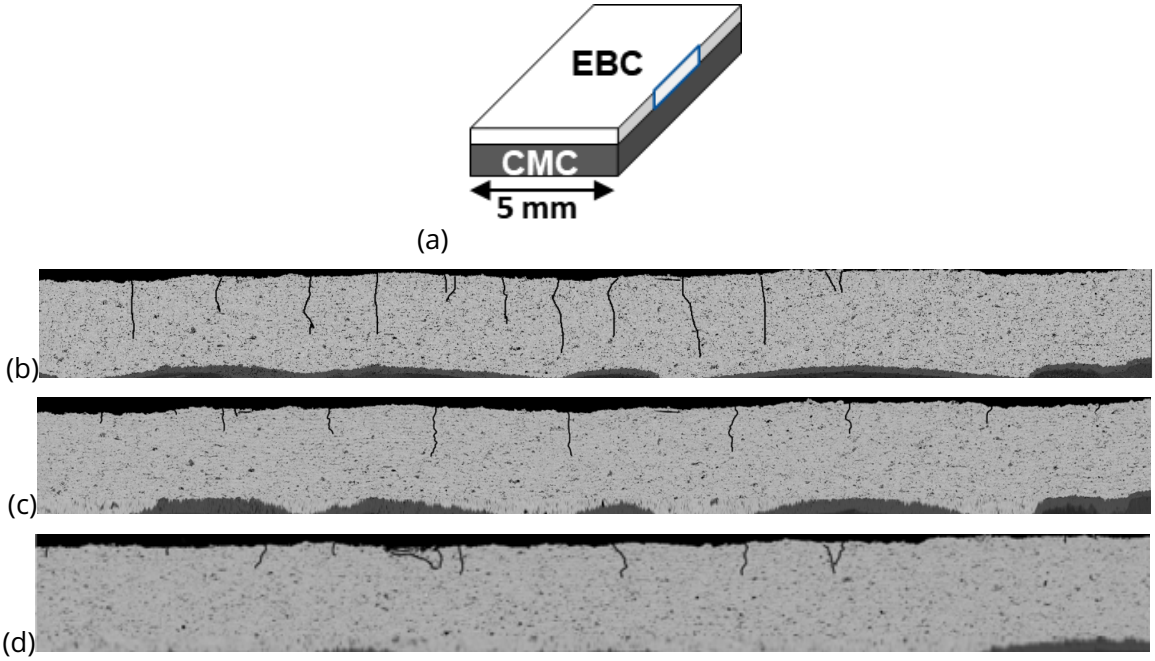

Figure 20: (a) Cross-section SEM observations for different cooling durations. (b) Almost instantaneous, (c) 15 min, (d) 2 h durations.

Varying the cooling duration confirmed that damage was occurring during this stage. By slowing down cooling, it was shown that the cracking events occurred with a time delay. Slowing down cooling was also linked to a less extended network and a slightly increased number of closed cells. However, the strongest impact was on the depth of the network.

3.5 Impact of coating thickness

It is known that increasing the temperature of aeroplanes engines improves their efficiency [35]. Yet, this increase is limited to the substrate capability. In order to improve the operating temperature of hot-section components, the thickness of the coating can be used as a thermal barrier. The thicker the coating, the lower the temperature at the surface of the CMC. Unfortunately, there are also some disadvantages: (i) it adds extra weight to CMC components, (ii) it increases residual stresses in the CMC/EBC system and (iii) the thermal gradient through the thickness of the coating becomes higher. Therefore, the influence of the thickness of the coating on the damage mechanisms was characterized.

In the previous cases, the coating thickness was set to 1000 µm. To determine the impact of the coating thickness on cracking, a system with a thinner coating (300 µm) was evaluated. The maximum temperature was 1250°C, the mechanical load 9 kg and the laser was turned off instantaneously at the end of the thermal stage.

Temperature field at the coating surface

The temperature field generated at the surface of the samples was also used to investigate the impact of the coating thickness (figure 21). In the central area of the coating surface, the temperature level was the same for both system thicknesses. However, the temperature gradient across the thickness was different.

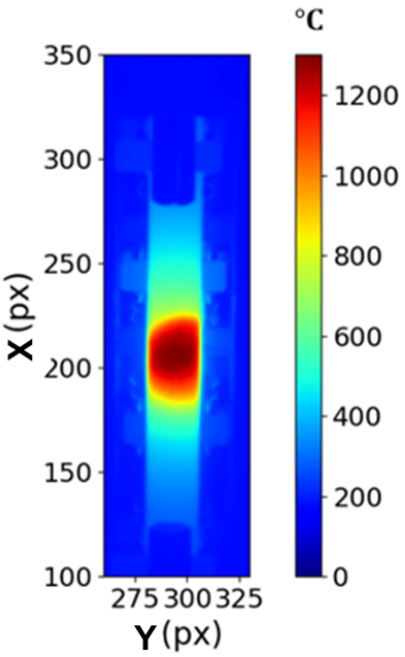

Figure 21: Temperature field at the coating surface for a maximum temperature level of 1250°C.

In fact, it appears that the temperature difference was greater in the thicker system than in the thinner one (figure 22). As a result, the thermal gradient induced in the thinner coating was smaller than that in the thicker coating, both along the length of the specimen and in the thickness of the system.

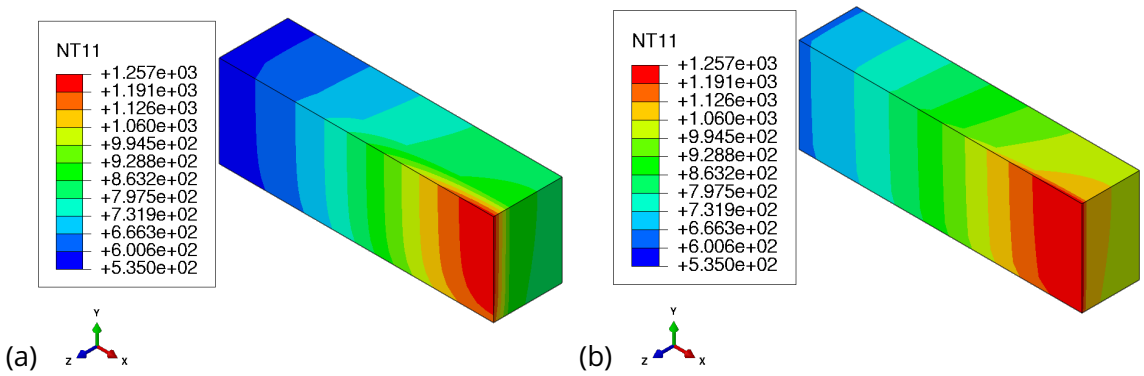

Figure 22: Computed temperature fields for a coating of (a) 1000 µm and (b) 300 µm.

Acoustic emission

No acoustic events were detected during the test on the 300 µm coating, thereby indicating the absence of damage in the system.

SEM observations

SEM observations of the coating surface (figure 23(a)) highlight the formation of the crack network for the thickest system (figure 23(b)) but not for the thinnest system (figure23(c)). This observation confirmed the results obtained from the acoustic emission analysis. For the same mechanical load, more damage would have been expected on the thinner system. However, for the same surface thermal loading, the thermal gradients induced in the thickness were different. In the case of a thin coating, the gradients were less significant than for a thick coating. However, coating cracking was mainly due to thermal gradients, since this type of damage was not possible at uniform temperatures. This difference in thermal gradients through the thickness explains the previous observations.

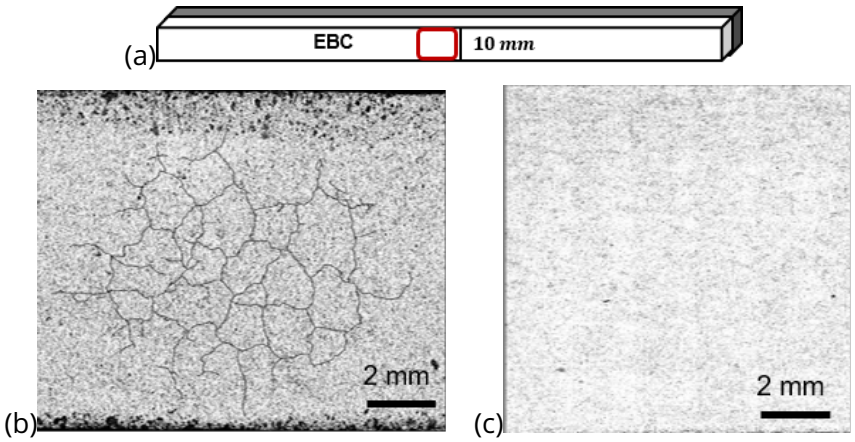

Figure 23: (a) Central area of the coating surface observed by SEM after the first thermomechanical loading cycle for a thickness of (b) 1000 µm and (c) 300 µm.

4 Discussion

The loading parameters such as mechanical load (inducing various stress levels) and temperature levels were chosen to impact creep activation and the creep strain level. The cooling duration was also studied to see its impact on creep. Last, the coating thickness (geometric parameter) was chosen to assess its influence for industrial applications. In the case of a 1 mm coating, both mechanical loads induced a (longitudinal) stress level of 15 MPa. Four of the five investigated parameters had a strong influence on coating cracking (summarized in figure 24). First, the temperature was set to 1250°C in order to be in the most favorable configuration for the development of a crack network. When the level of mechanical load was varied, it had a direct impact on the network shape. A circular network driven by the shape of the Gaussian for a mechanical load of 9 kg changed into a network composed of

a circular part with cracks crossing the full width of the sample. The through cracks were more critical for the performance of the system since they reached the interface with the CMC while the cracks of the circular network remained confined to the top of the coating. This phenomenon was explained by the biaxial stress state in the system. When the mechanical loading was "low" (0 or 9 kg), the stress state was mainly driven by the thermal loading and more specifically by the shape of the thermal loading. Thus, the resulting crack network was circular. When the mechanical load was increased (above a certain threshold), the stress state became driven by the latter, which resulted in a change in the shape of the network with the onset of flexural cracks across the width of the sample.

Case	*Cell number*	*Average cell diameter*	*Extension*	*Network shape*	*Propagation*
Thickness 1 mm Mechanical load 0 kg Maximum temperature 1250°C Cooling duration instantaneous	*9*	*1.5 mm*	*6.3 x 6.3 mm*	*Circular*	*confined within the coating surface*
Thickness 1 mm Mechanical load 9 kg Maximum temperature 1250°C Cooling duration instantaneous	*13*	*1.5 mm*	*8.1 x 8.1 mm*	*Circular*	*confined within the coating surface*
Thickness 1 mm Mechanical load 11 kg Maximum temperature 1250°C Cooling duration instantaneous	*3*	*2.5 mm*	*8.1 x 10 mm*	*Circular + through crack*	*crack reaching the interface*
Thickness 1 mm Mechanical load 9 kg Maximum temperature 1100°C Cooling duration instantaneous	*0*	*0*	*4.2 x 4.2 mm*	*incomplete network*	*confined within the coating surface*
Thickness 1 mm Mechanical load 9 kg Maximum temperature 1250°C Cooling duration instantaneous laser beam case (b)	*19*	*2 mm*	*10.6 x 9 mm*	*Circular*	*confined within the coating surface*
Thickness 1 mm Mechanical load 9 kg Maximum temperature 1250°C Cooling duration 15 min	*22*	*1.5 mm*	*10.4 x 9 mm*	*Circular*	*confined within the coating surface*
Thickness 1 mm Mechanical load 9 kg Maximum temperature 1250°C Cooling duration 2 h	*23*	*1.5 mm*	*9.2 x 8.3 mm*	*Circular*	*confined within the coating surface*
Thickness 0.3 mm Mechanical load 9 kg Maximum temperature 1250°C Cooling duration instantaneous	*0*	*0*	*0*	-	-

Figure 24: Summary of the different types of cracking patterns.

The maximum temperature was directly related to the intensity of the crack network. For a given geometry, the higher the temperature, the higher the crack density. Temperature was one of the key parameters of the creep law that activated this mechanism [27]. Thus, the higher the temperature, the higher the creep level. Moreover, the higher the maximum

temperature of the center point, the larger the area exceeding a temperature threshold activating creep. Therefore, the higher the creep level over a large area, the richer the crack network will be. This trend was particularly highlighted in figure 13. The more extensive the area where temperature exceeded 1000°C, the more developed the crack network. This result was mainly due to creep. Moreover, with the thermal cycle parameters of this study and analyzing the temperature fields related to the crack networks, a minimum temperature of 1100°C was necessary to reach creep strain levels responsible of the crack onset.

For the selected specimen dimensions, the variation in shape of the laser beam did not have a strong influence on the crack network since the central zone above 1100°C was almost the same in both cases. This observation suggested that the two samples would have crept in the same way, which led to a similar crack network in both cases.

For all cases, damage always occured during cooling. This observation was explained by the tensile stress state through the EBC layer [34]. The crack networks shown on the surface (figure 19) and through the thickness of the coating (figure 20) highlighted a tensile stress state that was generated through the coating, from its surface, during cooling. This stress state was strongly related to the creep strain depending on temperatureand time but also to the inversion of the thermal gradient at the center of the coating surface when the cooling started [17, 19]. Thus, the onset of damage was related to the cooling duration. In contrast, the shape of the network was not influenced by the cooling duration. The cooling duration directly impacted the depth of the network, namely, the faster the cooling, the deeper the network.

The thickness of the coating played an important role in cracking of the system. For a thin coating, it was impossible to generate damage. Although in both cases the same thermal and mechanical loads were applied, varying the thickness of the system meant that temperature diffusion did not occur in the same way in both cases because of the specimen geometry (300 µm versus 1000 µm). There were lower temperature gradients in the thinner coating than in the thicker one. There was less diffusion because less heat loss through the thickness. This difference induced a lower thermomechanical stress in the thin coating. Since the stress level controls creep, this observation explained that the thin coating did not crack.

Last, the stress levels reached in the case of a 1 mm coating (with or without mechanical loading) provide an additional explanation of the cracking observed on the surface of the coating. By setting a damage threshold of 110 MPa (equivalent to 0.1% strain [30]), figure 25, captured at the beginning of cooling, shows that this threshold was exceeded in the central area.

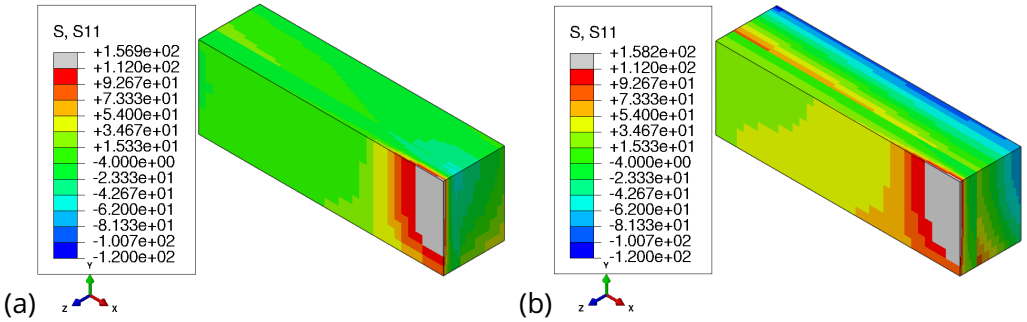

Figure 25: Maximum principal stress field (MPa) during cooling, at the time step when the stress is highest, (a) under thermal loading only and (b) under coupled thermomechanical loading.

5 Conclusion

This paper proposed to analyze the failure mechanisms of an EBC coated SiC/SiC composite under thermal gradient and mechanical loading. The following conclusions were drawn:

- The mechanical load has an influence on the shape of the network and its depth. The higher the mechanical load, the more the shape of the network will be driven by flexural stresses and not the Gaussian thermal loading. Moreover, cracks induced by flexural loading (i.e. crossing the width of the specimen) reached the interface of the system and therefore represented a privileged path for the penetration of oxidizing species at high temperatures in engine environments.

- The temperature gradients and level, and therefore the creep level of the coating, had a direct impact on the formation of crack networks. Numerically, this observation was confirmed by finite element analyses to study the evolution of the principal creep strain. The level of the creep strain over one cycle was larger at the highest temperature. Experimentally, the crack network due to thermal loading at 1250°C was larger in terms of cell number and extent than that obtained with a thermal loading at 1100°C. Moreover, the size of the network depended on the area that exceeded a sufficiently high temperature threshold. It should be noted that in this study, none of the vertical cracks developed into delamination cracks at the CMC/EBC interface.

- The cooling duration delayed the initiation of damage but did not impact the crack network shape. However, it had a strong effect on the depth of the network. The slower the cooling, the shallower the network.
- The thickness of the coating played an important role on damage. The thinner the coating, the less dense the network. When the thickness of the coating becomes thin enough, the damage threshold is not reached anymore.

The impact of all these parameters on the failure mechanisms of the CMC/EBC system was related to the stress level resulting from different loading conditions. The whole study of the formation of the network is an additional work that does not fall within the scope of the article. It would be interesting to set up a crack propagation model to explain the different cases observed experimentally.

6 Acknowledgements

This work was supported under ATLAAS, French research project co-funded by DGAC, ONERA and SAFRAN Group, involving SAFRAN Group, ONERA and CNRS.

7 Appendix 1: Model parameters

CMC radiation coefficients are shown in the following table:

Coefficient ($W.m^{-2}.K^{-4}$)	Temperature (°C)
0.02	600
0.06	1000
0.14	1400

EBC radiation coefficients are shown in the following table:

Coefficient ($W.m^{-2}.K^{-4}$)	Temperature (°C)
0.042	694.5
0.05	803.5
0.05	900
0.06	1000
0.07	1100
0.09	1200
0.1	1300
0.12	1400

The convective exchange coefficients for CMC are shown in the following table:

Coefficient ($W.m^{-2}.K^{-1}$)	Temperature (°C)
0.004	600
0.005	800
0.005	1000
0.005	1200
0.005	1400
0.005	1500

The convective exchange coefficients for EBC are shown in the following table:

Coefficient ($W.m^{-2}.K^{-1}$)	Temperature (°C)
0.009	600
0.01	700
0.01	800
0.011	900
0.011	1000
0.011	1100
0.011	1200
0.012	1300
0.012	1400

The thermomechanical properties of CMC are shown in the following table:

$E_{11}E_{22}$	$275\ GPa$
E_{33}	$130\ GPa$
G_{12}	$96\ GPa$
$G_{13}G_{23}$	$87\ GPa$
ν	$0,2$
Thermal expansion	$4,5.10^{-6}C^{-1}$

The thermomechanical properties of EBC are shown in the following table:

E	$112\ GPa$
ν	$0,22$
Thermal expansion	$4,21.10^{-6}C^{-1}$

EBC creep parametes used are shown in the following table:

n	$1,22$
m	$0,79$

References

[1] P. Spriet, Ceramic Matrix Composites – Materials, Modeling and Technology. *ch. CMC Applications to Gas Turbines,* pp. 591–608, 2014

[2] D. B. Marshall, B. N Cox, Integral textile ceramic structures. *Annual Review of Materials Research,* vol. 38, pp. 425-443, 2008

[3] J. A. Dever, M. V. Nathal, J. A. Dicarlo, Research on high-temperature aerospace materials at NASA Glenn Research Center. *Journal of Aerospace Engineering,* vol. 26, pp. 500-514, 2013

[4] P. J. Meschter, E. J. Opila, N. S. Jacobson, Water vapor–mediated volatilization of high-temperature materials. *Annual Review of Materials Research,* vol. 43, pp. 559-588, 2013

[5] K. N. Lee, D. S. Fox, J. I. Eldridge, D. Zhu, R. C. Robinson, C. Raymond, N. P. Bansal, R. A. Miller, Upper temperature limit of environmental barrier coatings based on mullite and BSAS. *Journal of the American Ceramic Society,* vol. 86, pp. 1299-1306, no. 8, 2003

[6] K. N. Lee, D. S. Fox, N. P. Bansal, Rare earth silicate environmental barrier coatings for SiC/SiC composites and Si3N4 ceramics. *Journal of the European Ceramic Society,* vol. 25, pp. 1705-1715, no. 10, 2005

[7] S. Ueno, T. Ohji, HT. Lin, Recession behavior of a silicon nitride with multi-layered environmental barrier coating system. *Ceramics international,* vol. 33, pp. 859-862, no 5, 2007

[8] S. Ueno, T. Ohji, HT. Lin, Corrosion and recession of mullite in water vapor environment. *Journal of the European Ceramic Society,* vol. 28, pp. 431-435, no 2, 2008

[9] Y. Okita, Y. Mizokami, J. Hasegawa, Jun, Experimental and numerical investigation of environmental barrier coated ceramic matrix composite turbine airfoil erosion. *Journal of Engineering for Gas Turbines and Power,* vol. 141, no 3, 2019

[10] K. M. Grant, S. Krämer, G. GE. Seward, C. G. Levi, Calcium–magnesium alumino-silicate interaction with yttrium monosilicate environmental barrier coatings. *Journal of the American Ceramic Society,* vol. 93, pp. 3504-3511, no 10, 2010

[11] W. D. Summers, D. L. Poerschke, D. Park, J. H. Shaw, F. W. Zok, C. G. Levi, Roles of composition and temperature in silicate deposit-induced recession of yttrium disilicate. *Acta Materialia,* vol. 160, pp. 34-46, 2018

[12] H. Zhao, B. T. Richards, C. G. Levi, H. NG. Wadley, Molten silicate reactions with plasma sprayed ytterbium silicate coatings. *Surface and Coatings Technology,* vol. 288, pp. 151-162, 2016

[13] R. T. Bhatt, S. R. Choi, L. M. Cosgriff, D. S. Fox, K. N. Lee, Impact resistance of environmental barrier coated SiC/SiC composites. *Materials Science and Engineering: A,* vol. 476, pp. 8-19, no 1-2, 2008

[14] K. A. Kane, E. Garcia, S. Uwanyuze, M. Lance, K. A. Unocic, S. Sampath, B. A. Pint, Steam oxidation of ytterbium disilicate environmental barrier coatings with and without a silicon bond coat. *Journal of the American Ceramic Society,* vol. 104, pp. 2285-2300, no 5, 2021

[15] N. Rohbeck, P. Morrell, P. Xiao, Ping, Degradation of ytterbium disilicate environmental barrier coatings in high temperature steam atmosphere. *Journal of the European Ceramic Society,* vol. 39, pp. 3153-3163, no 10, 2019

[16] K. -N. Lee, B. J. Puleo, D. L. Waters, G. Costa, Current EBC development and testing at NASA. *Technical Report, url=https://api.semanticscholar.org/CorpusID:131898503,* 2017

[17] D. Zhu, R. A. Miller, Influence of High Cycle Thermal Loads on Thermal Fatigue Behavior of Thick Thermal Barrier Coatings. *Technical report, National Aeronautics and Space Administration Cleveland OH Lewis Research,* 1997

[18] D. Zhu, R. A. Miller, Sintering and creep behavior of plasma-sprayed zirconia-and hafnia-based thermal barrier coatings. *Surface and Coatings Technology*, vol 108, pp. 114-120, 1998

[19] D. Zhu, R. A. Miller, Determination of creep behavior of thermal barrier coatings under laser imposed high thermal and stress gradient conditions. *Journal of materials research,* vol. 14, pp. 146-161, no. 1, 1999

[20] B. T. Richards, S. Sehr, F. de Franqueville, M. R. Begley, H. NG. Wadley, Fracture mechanisms of ytterbium monosilicate environmental barrier coatings during cyclic thermal exposure. *Acta Materialia* vol. 103, pp. 448-460, 2016

[21] Y. R. Takeuchi, K. Kokini, Thermal fracture of multilayer ceramic thermal barrier coatings. *Turbo Expo: Power for Land, Sea, and Air. American Society of Mechanical Engineers* vol. 78972, 1992

[22] K. Kokini, B. D. Choules, Y. R. Takeuchi, Thermal fracture mechanisms in ceramic thermal barrier coatings. *Journal of thermal spray technology* vol. 6, pp. 43-49, 1997

[23] A. Kawasaki, R. Watanabe, Thermal shock fracture mechanism of metal/ceramic functionally gradient materials. *Thermal Shock and Thermal Fatigue Behavior of Advanced Ceramics*, pp. 509-520, 1993

[24] H. Takahashi, T. Ishikawa, D. Okugawa, T. Hashida, Laser and plasma-ARC thermal shock/fatigue fracture evaluation procedure for functionally gradient materials. *Thermal Shock and Thermal Fatigue Behavior of Advanced Ceramics*, pp. 543-554, 1993

[25] D. Zhu, R. A. Miller, Investigation of thermal fatigue behavior of thermal barrier coating systems. *Surface and Coatings Technology* vol. 94, pp. 94-101, 1997

[26] A. Lacombe, P. Spriet, G. Habarou, E. Bouillon, A. Allaria, Ceramic Matrix Composites to Make Breakthroughs in Aircraft Engine Performance. *50th AIAA/ASME/ASCE/AHS/ASC Structures, Structural Dynamics, and Materials Conference*, pp 2675, 2009

[27] T. Archer, M. Berny, P. Beauchêne, F. Hild, Creep behavior identification of an environmental barrier coating using full-field measurements. *Journal of the European Ceramic Society,* vol. 40, pp. 5704-5718, no. 15, 2020

[28] D. L. May, A. P. Gordon, D. S. Segletes, The application of the Norton-Bailey law for creep prediction through power law regression. *Proceedings of ASME Turbo Expo 2013: Turbine Technical Conference and Exposition GT2013, June 3-7, 2013, San Antonio, Texas, USA*

[29] D. G. Eitzen, H. N. G. Wadley, Acoustic emission: establishing the fundamentals. *Journal of research of the National Bureau of Standards,*, pp. 75, no. 1, 1984

[30] D. Zhu, Development and Performance Evaluations of HfO2-Si and Rare Earth-Si Based Environmental Barrier Bond Coat Systems for SiC/SiC Ceramic Matrix Composites. *International Conference on Metallurgical Coatings and Thin Films,* NASA Glenn Research Center , 2014

[31] L. Yang, T. T. Yang, Y. C. Zhou, Y. G. Wei, R. T. Wu, N. G. Wang, Acoustic emission monitoring and damage mode discrimination of APS thermal barrier coatings under high temperature CMAS corrosion. *Surface and Coatings Technology,* vol. 304, pp. 272-282, 2016

[32] S. Momon, N. Godin, P. Reynaud, M. R'Mili, G. Fantozzi, Unsupervised and supervised classification of AE data collected during fatigue test on CMC at high temperature. *Composites Part A: Applied Science and Manufacturing,* vol. 43, pp. 254-260, no. 2, 2012

[33] B. T. Richards, D. Zhu, L. Ghosn, H. Wadley, Mechanical properties of air plasma sprayed environmental barrier coating (EBC) materials. *International Conference and Expo on Advanced Ceramics and Composites*, 2015

[34] B. D. Choules, K. Kokini, T. A. Taylor, Thermal fracture of ceramic thermal barrier coatings under high heat flux with time-dependent behavior: Part 1. Experimental results. *Materials Science and Engineering: A,* vol. 299, pp. 296-304, 2001

[35] H. Zhao, C. G. Levi, H. N. G. Wadley, Molten silicate interactions with thermal barrier coatings. *Surface and Coatings Technology*, 251 :74–86, July 2014